Polymorphism of Actin Paracrystals Induced by Polylysine

WALTER E. FOWLER and UELI AEBI
Department of Cell Biology and Anatomy, The Johns Hopkins University School of Medicine, Baltimore, Maryland 21205

ABSTRACT We describe a method for the induction of different polymorphic forms of actin filament paracrystals. This polymorphism is probably based on differences in the stagger and/or polarity of adjacent filaments in single-layered paracrystals and by superposition of different layers in multilayered paracrystals. The helical parameters defining the filament geometry are indistinguishable for the different polymorphic forms observed and for the four different actins used. Analysis of these paracrystals, some of which are ordered to better than 2.5 nm, should provide a reference structure suitable for alignment and orientation within the actin filament of high resolution models of the actin monomer obtained from crystal data.

Most, if not all, intracellular functions of the ubiquitous protein actin require that it be present in the form of filaments, which may be described as two right-handed helically wound strands of actin monomers. Although the molecular structures of muscle and nonmuscle actins are now being studied in detail from two- (P. R. Smith, W. E. Fowler, T. D. Pollard, and U. Aebi, manuscript in preparation) and three-dimensional (1) crystal data, understanding these molecular models in terms of the functionally significant filament will depend greatly on knowledge of their orientation within the filament, which in turn will require a sufficiently high-resolution (e.g., $\leq$ 2.5 nm) three-dimensional model of the filament as a reference structure. To date, the most detailed three-dimensional models of actin filaments (~3-nm resolution) have been determined from naturally occurring (2, 3) or synthetic (4–6) actin filament paracrystals. Paracrystalline arrays of either muscle or nonmuscle actin consist of actin filaments associated side-to-side with a defined rule relating the stagger and polarity of adjacent helical filaments. Naturally occurring paracrystals invariably involve "cross-linking" of actin filaments by accessory proteins (2, 3), and similar paracrystals can be reconstituted in vitro by adding cross-linking proteins to pure actin filaments (2, 7). Synthetic paracrystals can also be made from G- or F-actin or muscle thin filaments in the absence of cross-linking proteins by appropriately adjusting the ionic environment: the standard method for inducing actin filament paracrystals has long been the addition of 25–100 mM $MgCl_2$ to G- or F-actin (8), and more recently other divalent cations have been shown to be effective (9).

Polycations are known to induce actin polymerization and to cause lateral aggregation of the resulting filaments (10, 11). We have attempted to optimize the conditions for paracrystal formation and have found that polylysine, in the presence of 150–450 mM KCl, induces both muscle and nonmuscle actins to form actin filament paracrystals ordered to ~2.5 nm both axially and radially. These paracrystals exhibit an interesting polymorphism that can be explained by the variety of lateral associations of actin filaments that are mediated by polylysine.

MATERIALS AND METHODS

Materials

Polylysine hydrobromide (Type II, degree of polymerization 15–20) and protamine sulfate (Grade I) were obtained from Sigma Chemical Co. (St. Louis, MO). All other chemicals were reagent grade.

Proteins

Acanthamoeba and rabbit skeletal muscle actin were purified as described (12). Smooth muscle actin was extracted from an acetone powder of chicken gizzards and purified by two cycles of polymerization/depolymerization followed by gel filtration on Sephadex G-150. *Physarum* actin was purified as described (13).

Electron Microscopy

For electron microscopy, 2-μl drops were adsorbed for 60 s to carbon-coated 400-mesh grids which were rendered hydrophilic by glow discharge in a reduced atmosphere of air. The grids were then washed for 30 s on several drops of distilled water and stained for 30 s on several drops of 0.75% uranyl formate, pH 4.25. Electron microscopy was performed on a Zeiss EM10C electron microscope.

Determination of Helical Parameters

The parameters defining the helical geometry of the actin filament (given in Table I) were calculated from layer line altitudes Z_l (14) measured on optical diffraction patterns such as those shown in Fig. 4. These were indexed according to the "approximate" integer selection rule: $l = -6 \cdot n + 13 \cdot m$ describing the left-handed genetic helix which passes through all actin subunits of the double-helical filament (4, 6, 17). The following layer lines, when present, were included in our measurements: l = 1, 2, 5, 6, 7, 8, and 13, which sample the Bessel orders, n = 2,

THE JOURNAL OF CELL BIOLOGY · VOLUME 93 MAY 1982 452–458

4, −3, −1, 1, 3, and 0 belonging to the "diffraction branches," $m = 1, 2, -1, 0, 1, 2$, and 1. For each paracrystal diffracted, the "exact" non-integer selection rule $Z = a \cdot n + b \cdot m$ (14) was computed from the measured layer line altitudes Z_l by a least-squares procedure which minimized the following residual: $R = \Sigma_l (Z_l - a \cdot n_l - b \cdot m_l)^2$. The ratio b/a, which expresses the exact number of actin subunits per turn of the left-handed genetic helix (and which is independent of the micrograph magnification and diffraction constant used), was then calculated for each paracrystal.

Construction of Paracrystal Models

The paracrystal models shown in Fig. 3 were all constructed using four helical repeats of an average filament: these were obtained from a six filament wide stretch of a fuzzy-sharp paracrystal and were longitudinally averaged over the four helical repeats. This average filament was clearly polar, as determined by cross-correlation and three-dimensional reconstruction (data not shown). Single-layered paracrystals were built by periodically continuing a unit cell consisting of one or two adjacent filaments having a relative stagger of 0, ¼, or ½ of the long pitch helical repeat (37.5 nm). Two-layered paracrystals were constructed by superimposing two single layered paracrystals in a parallel fashion; the two layers had a relative stagger of 0, ¼, or ½ the long pitch helical repeat parallel to the filament axis and/or a lateral translation of either 0 or ½ the interfilament distance. All the filaments making up the paracrystal models have the same polarity and are parallel. Computing was performed on a PDP-11/34A minicomputer using a modular image processing software package adapted by Dr. B. L. Trus (15) from a software package developed earlier by Dr. P. R. Smith (16) and one of us (Dr. Aebi). Electron micrograph data collection and display were done on an Optronics P-1700 rotating drum film scanner/writer using programs written by Mr. E. L. Buhle in our laboratory.

RESULTS

Induction of Paracrystals

Addition of a 1:1 to 4:1 molar ratio of polylysine (3,000–4,000 mol wt) to 1 mg/ml muscle or nonmuscle G-actin results in an immediate development of turbidity. Inspection in the electron microscope shows thick bundles of filaments having no paracrystalline order. However, upon addition of KCl to a final concentration of 150–450 mM there is an immediate decrease in turbidity; electron microscope examination of this material reveals the formation of paracrystals. These paracrystals (Fig. 1) grow over a period of several days, either at room temperature or at 0°C. By electron microscopy, the optimal salt concentration for paracrystal formation was found to be 250–400 mM KCl: below 100 mM KCl only bundles were seen and above 500 mM KCl only filaments were found. Paracrystals can also be induced from F-actin formed in 150–400 mM KCl by subsequently adding polylysine. In our hands, polylysine/KCl induction yields a 3- to 10-fold higher ratio of paracrystalline to nonparacrystalline material (i.e., filament bundles) than Mg^{++}-induction.

To test the polycation specificity of paracrystal induction, we repeated the experiments described above with polylysine replaced by protamine sulfate (~4,100 mol wt) or by spermine tetrachloride (348 mol wt). At a 1:1 protamine:actin molar ratio and 350 mM KCl, paracrystals similar to those induced by polylysine were obtained (data not shown). In contrast, although the spermine:actin molar ratio was varied from 1:1 to 7:1, only filaments and a few small filament bundles were formed and no paracrystals were found.

Polymorphism

We have used polylysine/KCl induction to obtain paracrystals of two muscle actins (rabbit skeletal muscle and chicken gizzard smooth muscle) and two nonmuscle actins (*Acanthamoeba* and *Physarum*). Paracrystals made from each actin type exhibit a range of morphologies: some are common to paracrystals formed from all four types of actin and some are limited to paracrystals made from nonmuscle actins. Several of the polymorphic forms are shown in Figs. 1 and 2. Paracrystals formed from nonmuscle actin using this induction method most often display the morphology shown in Fig. 1 *a*. Muscle actin paracrystals exhibiting a variety of morphologies are shown in Fig. 1 *b*. Although both nonmuscle actins tried can form paracrystals with any of the morphologies shown in Fig. 1, the two muscle actins used apparently do not form paracrystals with the "fuzzy-sharp" morphology shown in Fig. 1 *a* when induced by polylysine/KCl. In fuzzy-sharp paracrystals (Fig. 1 *a*), adjacent filaments within a layer have their helices approximately in register (i.e., no apparent stagger), giving rise to the alternating fuzzy and sharp banding patterns along the paracrystal axis. This type of morphology is commonly observed both in naturally occurring actin arrays (2, 19) and in Mg^{++}-induced paracrystals from either muscle or nonmuscle actin.

A gallery of paracrystals, all of which were formed under the same induction conditions, is shown in Fig. 2 (*a–d*, nonmuscle actin; *e–h*, muscle actin). Some of the paracrystal morphologies shown here involve a systematic stagger of adjacent filaments: such a stagger can sometimes be seen directly be sighting along the paracrystal axis at an oblique angle (see e.g., Fig. 2 *b* and *f*). The magnitude of the stagger may vary from paracrystal to paracrystal and even within one paracrystal (e.g., Fig. 2 *b*). More complex polymorphic forms (e.g., Fig. 2 *c*, *d*, *g* and *h*) often display diagonal striations or diamondlike patterns, suggesting that some of the constituent filaments may be angled relative to the paracrystal axis. Alternatively, since these paracrystals are mostly multilayered, such morphologies may be derived from superposition of two or more layers of actin filaments. We have investigated the latter possibility by building two-layered paracrystal models, some of which are shown in Fig. 3. We found that each type of paracrystal morphology observed (Fig. 2, shown at higher magnification in Fig. 3) can be constructed from one or two layers of actin filaments. In each model, all the constituent filaments run parallel to the paracrystal axis and have the same polarity within and between layers of filaments; only a limited number of different staggers between adjacent filaments within one layer (i.e., 0, ¼, or ½ helical repeat) and lateral translations between the two layers (i.e., either 0 or ½ the interfilament distance) was required to simulate all the paracrystal morphologies shown in Figs. 2 and 3 (see Materials and Methods). Optical diffraction patterns of the models were consistent with those of the respective micrographs (data not shown; see below).

Optical Diffraction Analysis

To accurately measure the average helical parameters of filaments in paracrystals and to obtain information about the packing of filaments in the polymorphic paracrystal forms, micrographs were analyzed by optical diffraction. The average helical parameters defining the filament geometry for the four actins used were found to be remarkably similar to each other (Table I). The left-handed genetic helix contains on average -2.160 ± 0.003 actin monomers per turn; the same average value was found for the different polymorphic forms observed within each type of actin. This value is close to certain other reported values (17, 18) and is almost midway between the values expected for helices having integer selection rules consisting of 13 subunits in 6 turns ($b/a = 2.167$) or 28 subunits in 13 turns ($b/a = 2.154$), which are the two extremes of reported values (2, 4, 7, 19–21). The standard deviations, which are less

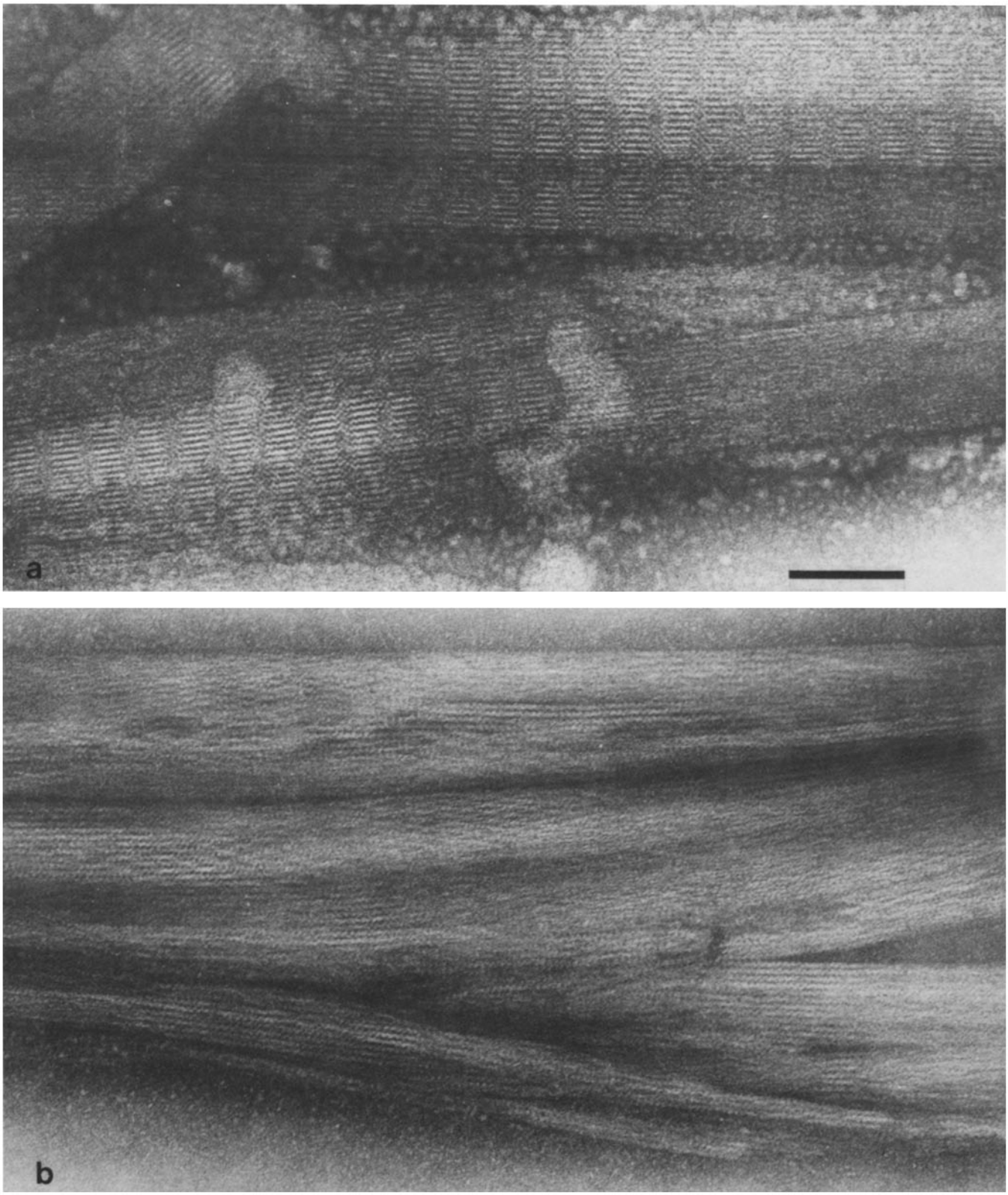

FIGURE 1 Electron micrographs of actin paracrystals induced by polylysine/KCl (see text and caption to Fig. 2) showing representative paracrystal morphologies for nonmuscle actin (*a*) and for muscle actin (*b*). (*a*) These paracrystals of *Acanthamoeba* actin exhibit the same "fuzzy-sharp" morphology that is prevalent in Mg^{++}-induced paracrystals. This morphology is also seen in *Physarum* actin paracrystals, but not in muscle actin paracrystals induced by polylysine/KCl. (*b*) These skeletal muscle actin paracrystals exhibit the polymorphism of paracrystals induced by polylysine/KCl, which is also seen with nonmuscle actin paracrystals. Bar, 100 nm. × 200,000.

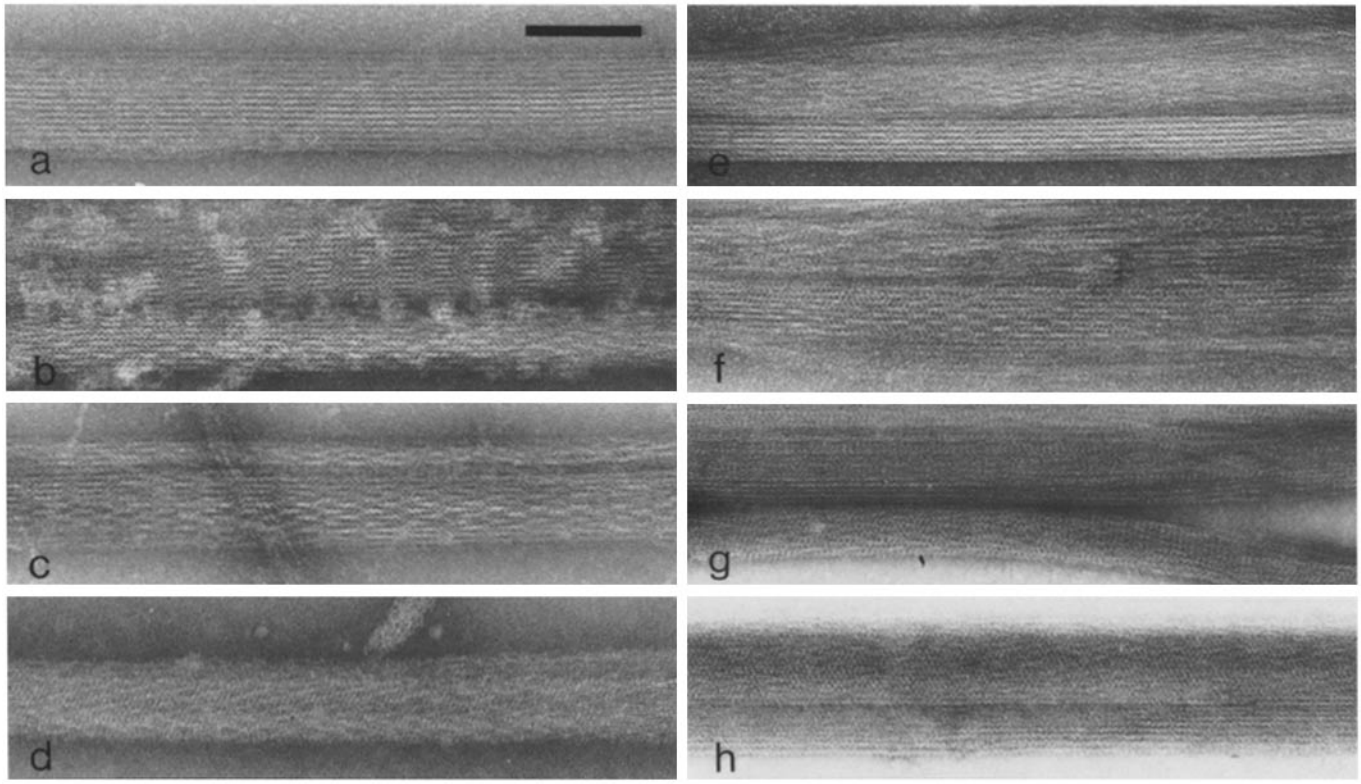

FIGURE 2 Gallery of electron micrographs showing examples of morphologies exhibited by paracrystals formed from nonmuscle actins (*a–d*) or muscle actins (*e–h*). All of these paracrystals were induced with a polylysine:actin molar ratio of 1:1 and 250–400 mM KCl. The appearance of these different morphologies is not dependent on the exact salt concentration within this range. Bar, 100 nm. × 150,000.

than or equal to those reported in similar studies (3, 7, 19, 20, 22), probably reflect slight distortions occurring during specimen preparation and/or electron irradiation rather than indicating inherent differences between filaments. Such variations even occur along the length of single paracrystals (data not shown).

Optical diffraction patterns of the different polymorphic forms of actin paracrystals induced by polylysine/KCl are of two distinct types, which are shown in Fig. 4 and are characterized by the presence (right side of diffraction patterns) or absence (left side of diffraction patterns) of intermediate row lines (20, 21, 23) (indicated in Fig. 4). The intermediate row lines arise from a spacing of twice the interfilament distance and thus indicate that the lateral repeating unit consists of two adjacent filaments, as is the case when adjacent filaments are staggered and/or have opposite polarity (20, 21). For example, the intermediate row lines in the right half of the diffraction pattern in Fig. 4*a* may be related to the apparent stagger of filaments on the right-hand side of the paracrystal in Fig. 4*a*. The left half of this diffraction pattern, which is from the fuzzy-sharp region on the left side of the paracrystal containing filaments that are "in-register," has no intermediate row lines. In Fig. 4*b*, differences between adjacent filaments that are imperceptible by eye are clearly revealed by optical diffraction. A slight stagger and/or the alternating polarity of adjacent filaments in the paracrystal on the right may give rise to the distinctive intermediate row lines (right half of diffraction pattern), whereas a paracrystal with a similar morphology (left) may have no intermediate row lines (left half of diffraction pattern). Diffraction studies of single-layered paracrystal models (data not shown) indicate that while staggers ranging in magnitude from ½ to 1/72 of a helical repeat, with or without alternating polarity of adjacent filaments, will cause the appearance of intermediate row lines, only double-layered paracrystal models (e.g., Fig. 3*c*) can correctly simulate the observed intensities of the second and seventh layer lines.

DISCUSSION

Filaments of the four different actins each have very similar helical parameters and statistical distributions of values (Table I), indicating that the helical geometry of the average actin filament is conserved in these paracrystals. Optical diffraction of single filaments masked out of different paracrystals confirms the invariance of actin filament geometry under these conditions, which contrasts with the remarkable differences in morphology exhibited by the paracrystals themselves. Since the helical parameters of the different polymorphic forms for a particular actin/cation combination are insignificantly different from each other, it is unlikely that the polymorphism shown here is related to a change or polymorphism in the actin helix, such as that which is induced in thin filament paracrystals by calcium (20) or that shown to occur in the filamentous bundle of the acrosomal process (22).

The difference between muscle and nonmuscle actins with regard to the formation and/or stability of fuzzy/sharp paracrystals is an unexpected finding but is consistent with other results that demonstrate subtle differences in the properties of these two classes of actins, such as affinity for muscle tropomyosin (24) and the ability to form crystalline actin sheets (12, 25, 26). Our finding may reflect differences in the distribution

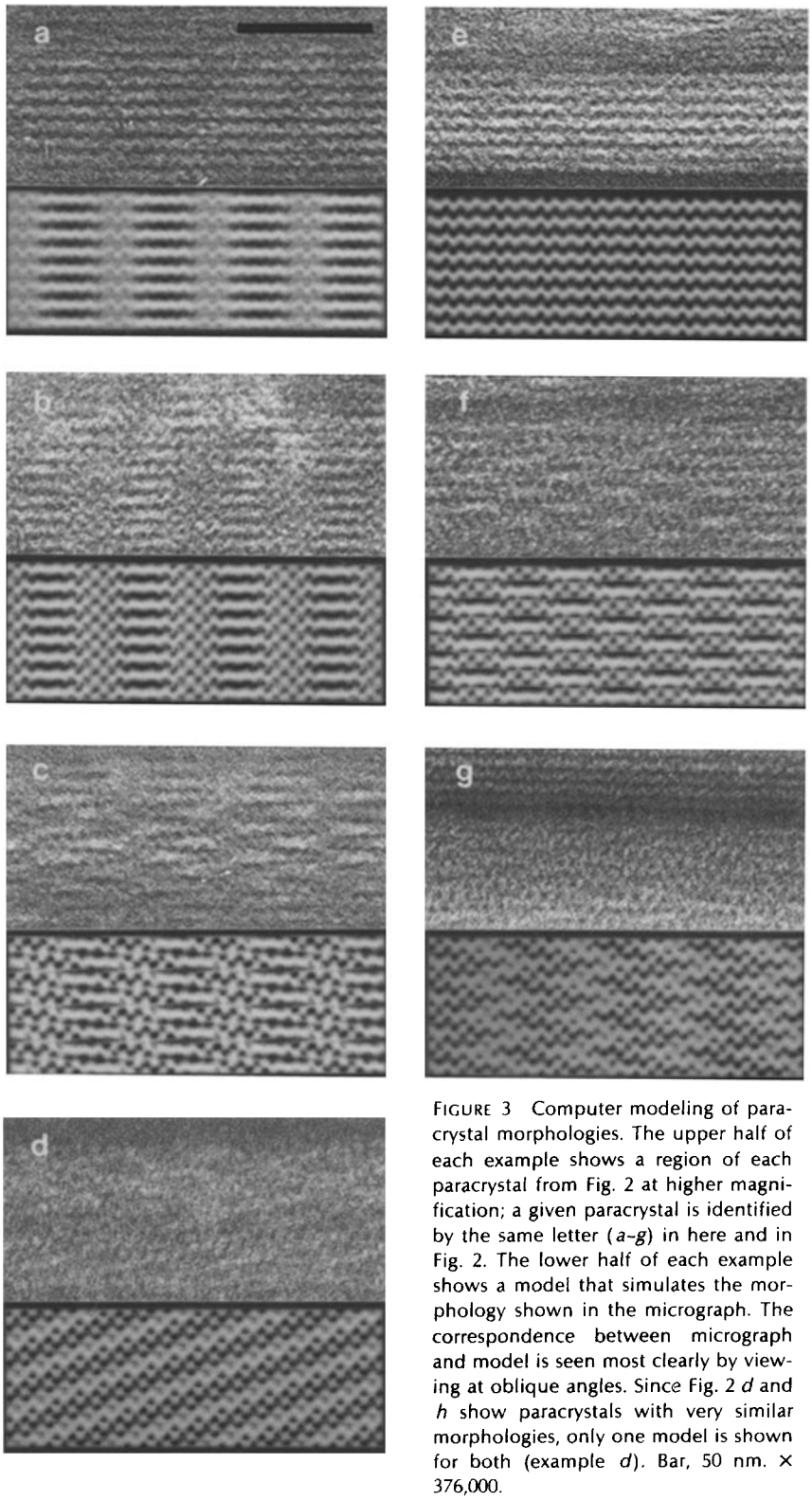

FIGURE 3 Computer modeling of paracrystal morphologies. The upper half of each example shows a region of each paracrystal from Fig. 2 at higher magnification; a given paracrystal is identified by the same letter (*a–g*) in here and in Fig. 2. The lower half of each example shows a model that simulates the morphology shown in the micrograph. The correspondence between micrograph and model is seen most clearly by viewing at oblique angles. Since Fig. 2 *d* and *h* show paracrystals with very similar morphologies, only one model is shown for both (example *d*). Bar, 50 nm. × 376,000.

of charged residues on the surface of the actin filament or small differences in mass distribution at regions of interfilament contact without significant changes in the parts of the actin molecule involved in intrafilament contacts. Other explanations are possible as well.

The paracrystal polymorphism described here can be explained by recognizing that a variety of lateral associations of actin filaments are mediated by polylysine. Specifically, the stagger of adjacent filaments is variable between different polylysine-induced paracrystals and occasionally within a given paracrystal. In addition, this type of paracrystal mostly contains more than one layer of actin filaments. With these rules in mind, we have been able to construct models which simulate every type of observed paracrystal morphology (Fig. 3). These models were made using the same "averaged" filament and thus do not require any changes in the helical

TABLE I

Helical Parameters

Actin/Induction	b/a	P_G[Å]	d[Å]	N
Acanthamoeba/polylysine	−2.15934 ± 0.00285 −2.15385/−2.16883	27.6 ± 0.2/27.514	58.3 ± 2.1	30
Acanthamoeba/Mg^{++}	−2.15941 ± 0.00492 −2.15365/−2.16864	— /27.513	54.8 ± 2.3	10
Physarum/polylysine	−2.16108 ± 0.00246 −2.15324/−2.17181	27.4 ± 0.2/27.492	58.8 ± 1.4	10
Rabbit skeletal muscle/polylysine	−2.16217 ± 0.00362 −2.15718/−2.16667	27.3 ± 0.2/27.478	59.1 ± 0.7	12
Chicken gizzard smooth muscle/polylysine	−2.16016 ± 0.00372 −2.15459/−2.16714	— /27.504	56.7 ± 0.9	14

The mean standard deviation and the maximum and minimum values of b/a (see Materials and Methods) are tabulated for a set of N measurements of each actin/cation combination. P_G, the axial repeat of the actin monomer along the genetic helix, has been calculated from the layer line altitudes Z_{13} when present, sampling the first meridional reflection corresponding to the genetic helix. It is tabulated as the mean with its standard deviation. This parameter has also been calculated by using the average of the exact helical selection rule as determined above for each actin/cation combination; this calculated value is given following the measured value. *d*, the average interfilament distance within the paracrystals, was calculated from the average radial distance of the first or second row lines in the diffraction patterns. It is given as the mean with the standard deviation for each set of measurements. *N* is the number of paracrystals included in each set of measurements for the different actin/cation combinations. Average values obtained by subdividing measurements within a given actin/cation combination in terms of paracrystal morphology were not significantly different from those given.

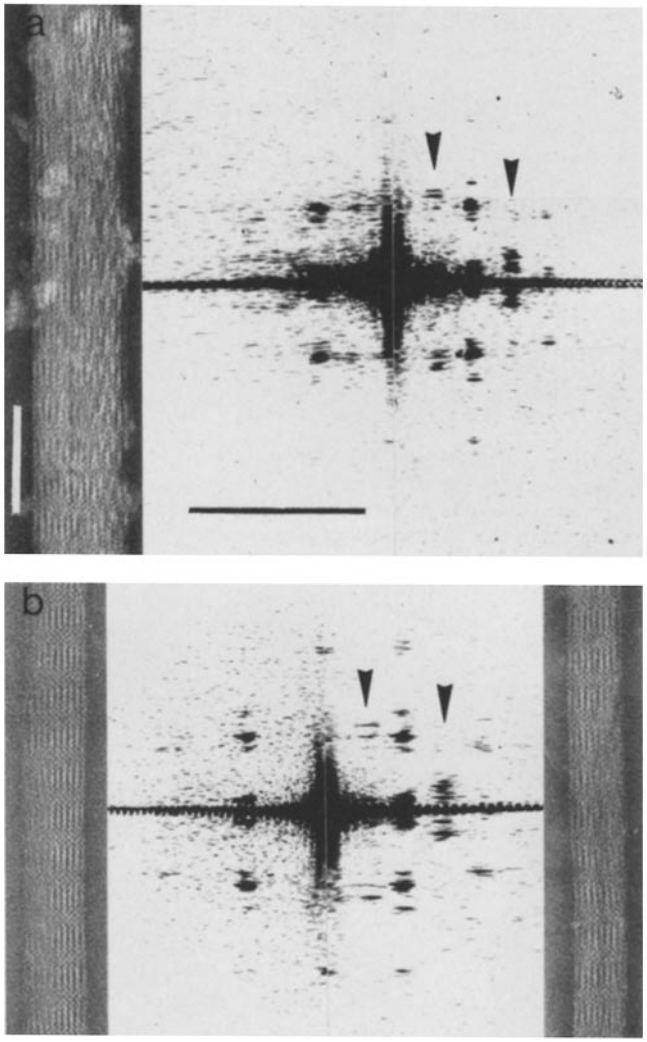

FIGURE 4 Electron micrographs and optical diffraction patterns of paracrystals formed from nonmuscle actin. (*a*) A single paracrystal exhibiting different morphologies on its left and right sides: the left and right halves of the diffraction pattern are from the left and right sides of the paracrystal, respectively. Note the intermediate row lines (arrowheads) on right half of diffraction pattern. (*b*) Two paracrystals formed under identical conditions which have similar morphologies but distinct diffraction patterns: the left and right halves of the diffraction pattern are from the paracrystals on the left and right, respectively. Note the intermediate row lines (arrowheads) on the right half of the diffraction pattern and their absence on the left half. Although the paracrystal on the right appears heterogeneous along its length, different regions of the area shown yield identical diffraction patterns. Bars: micrographs, 100 nm; diffraction patterns *a* and *b*, $(2.5\ nm)^{-1}$. Micrographs, × 150,000.

parameters of the actin filament. It is also important to note that all the filaments in the models are parallel and have the same polarity. Although these modeling studies do not prove that these packing arrangements exist in polylysine-induced paracrystals, they do show that a combination of staggers and superposition is sufficient to mimic the observed polymorphism, including the two types of optical diffraction patterns (Fig. 4).

Motivated by the work of O'Brien et al. (23) in determining the polarity of adjacent filaments in thin filament paracrystals, we have conducted experiments involving the decoration of polylysine-induced paracrystals with myosin subfragment-1. Our experiments indicate that these actin paracrystals contain filaments with both polarities occurring with about the same frequency (data not shown). However, due to the multilayered nature of polylysine-induced paracrystals, the polarity of adjacent filaments within a single layer could not be resolved unambiguously in these experiments. We hope that image reconstruction of paracrystals induced by the method described here, some of which are ordered to at least 2.5 nm both axially and radially, will yield a model of the actin filament with sufficient detail to allow visualization of the subunit polarity directly. Image reconstruction of a multilayered paracrystal may reveal the exact superposition geometry of adjacent layers of filaments, whereas reconstruction of a single filament to 2.5 nm resolution should provide the reference structure that is

needed to orient high-resolution models of the actin molecule within the actin filament.

We thank Dr. Mark Adelman for the *Physarum* actin, Mr. Loren Buhle for help with the computing, and Dr. Tom Pollard for critical reading of this manuscript.

This work was supported by a Muscular Dystrophy Association of America postdoctoral fellowship (to W. E. Fowler) and research grant (to U. Aebi), and National Institutes of Health Grant GM-27765 (to U. Aebi).

Received for publication 7 December 1981, and in revised form 9 February 1982.

REFERENCES

1. Suck, D., W. Kabsch, and H. G. Mannherz. 1981. Three-dimensional structure of the complex of skeletal muscle actin and bovine pancreatic DNase I at 6-A resolution. *Proc. Natl. Acad. Sci. U. S. A.* 78:4319–4323.
2. DeRosier, D. J., E. Mandelkow, A. Silliman, L. Tilney, and R. Kane. 1977. Structure of actin-containing filaments from two types of non-muscle cells. *J. Mol. Biol.* 113:679–695.
3. Spudich, J., and L. Amos. 1979. Structure of actin filaments from microvilli of sea urchin eggs. *J. Mol. Biol.* 129:319–331.
4. Moore, P., H. Huxley, and D. J. DeRosier. 1970. Three-dimensional reconstruction of F-actin, thin filaments and decorated thin filaments. *J. Mol. Biol.* 50:279–295.
5. Spudich, J., H. Huxley, and J. Finch. 1972. Regulation of skeletal muscle contraction. II. Structural studies of the interaction of the tropomyosin-troponin complex with actin. *J. Mol. Biol.* 72:619–632.
6. Wakabayashi, T., H. Huxley, L. Amos, and A. Klug. 1975. Three-dimensional image reconstruction of actin-tropomyosin complex and actin-tropomyosin-troponin T-troponin I complex. *J. Mol. Biol.* 93:477–497.
7. Castellani, L., and E. O'Brien. 1981. Structure of actin paracrystals induced by nerve growth factor. *J. Mol. Biol.* 147:205–213.
8. Hanson, J. 1973. Evidence from electron microscope studies on actin paracrystals concerning the origin of the cross-striation in the thin filaments of vertebrate skeletal muscle. *Proc. R. Soc. Lond. B. Biol. Sci.* 183:39–58.
9. Strzelecka-Golaszewska, H., E. Proshniewicz, and W. Drabikowski. 1979. Interaction of actin with divalent cations. 1. The effect of various cations on the physical state of actin. *Eur. J. Biochem.* 88:219–227.
10. Oriol-Audit, C. 1978. Polyamine-induced actin polymerization. *Eur. J. Biochem.* 87:371–376.
11. Brown, S., and J. Spudich. 1979. Nucleation of polar actin filament assembly by a positively charged surface. *J. Cell Biol.* 80:499–504.
12. Aebi, U., W. E. Fowler, G. Isenberg, T. Pollard, and P. R. Smith. 1981. Crystalline actin sheets: their structure and polymorphism. *J. Cell Biol.* 91:340–351.
13. Adelman, M. 1977. Physarum actin. Observations on its presence, stability, and assembly in plasmodial extracts and development of an improved purification procedure. *Biochemistry.* 16:4862–4871.
14. Smith, P. R., and U. Aebi. 1976. The determination of the helical screw angle of a helical particle from its diffraction pattern. *J. Mol. Biol.* 106:271–275.
15. Trus, B., and A. Steven. 1981. Digital image processing of electron micrographs—the PIC system. *Ultramicroscopy.* 6:383–386.
16. Smith, P. R. 1978. An integrated set of computer programs for processing electron micrographs of biological structures. *Ultramicroscopy.* 3:153–160.
17. DeRosier, D. J., and R. Censullo. 1981. Structure of F-actin from extracts of sea urchin oocytes. *J. Mol. Biol.* 146:77–99.
18. Tilney, L., D. J. DeRosier, and M. Mulroy. 1980. The organization of actin filaments in the stereocilia of cochlear hair cells. *J. Cell Biol.* 86:244–259.
19. Abe, S., R. Kamiya, and G. Eguchi. 1981. Actin paracrystal in the acrosome of newt sperm. *Exp. Cell Res.* 132:510–514.
20. Gillis, J., and E. O'Brien. 1975. The effect of calcium ions on the structure of reconstituted muscle thin filaments. *J. Mol. Biol.* 99:445–459.
21. O'Brien, E., J. Gillis, and J. Couch. 1975. Symmetry and molecular arrangement in paracrystals of reconstituted muscle thin filaments. *J. Mol. Biol.* 99:461–475.
22. DeRosier, D. J., L. Tilney, and P. Flicker. 1980. A change in the twist of the actin-containing filaments occurs during the extension of the acrosomal process in Limulus sperm. *J. Mol. Biol.* 137:375–389.
23. O'Brien, E., P. Bennett, and J. Hanson. 1971. Optical diffraction studies of myofibrillar structure. *Phil. Trans. R. Soc. Lond. B. Biol. Sci.* 261:201–208.
24. Yang, Y., E. Korn, and E. Eisenberg. 1979. Binding of tropomyosin to copolymers of Acanthamoeba actin and muscle actin. *J. Biol. Chem.* 254:2084–2088.
25. dosRemedios, C., and M. Dickens. 1978. Actin microcrystals and tubes formed in the presence of gadolinium ions. *Nature (Lond.).* 276:731–733.
26. Aebi, U., P. R. Smith, G. Isenberg, and T. Pollard. 1980. Structure of crystalline actin sheets. *Nature (Lond.).* 288:296–298.